Fatigue Modeling of a Powder Metallurgy Main Bearing Cap

Y. Hammi, T.W. Stone, P.G. Allison, and M.F. Horstemeyer

Center for Advanced Vehicular Systems (CAVS)
Mississippi State University
P.O. Box 5405
Mississippi State, MS 39762

Abstract: Developing the ability to predict density distribution, monotonic plasticity, damage and the cyclic damage progression is imperative for the design of Powder Metallurgy (PM) components that will experience overloads during in-service life due to impacts, rough ground, and crash environments. In this paper, mathematical-based models for PM manufacturing process are developed, validated and implemented in user material subroutines VUMAT and UMAT to model the compaction and sintering processes. The material history is initially captured and carried throughout the compaction and sintering processes in order to predict the density distribution. Knowing the density distribution, mechanical properties are mapped in the PM sintered part using tension, compression, and torsion mechanical tests performed on samples at different densities, temperatures and strain rates. A finite element analysis of an experimental fatigue fixture that reproduces similar loading conditions than those of in-service life conditions is performed. Using a Multi-Stage Fatigue (MSF) model implemented in Abaqus, the fatigue life is evaluated on a PM automotive component, the main bearing cap (MBC), and results are compared to experimental fatigue tests.

Keywords: Powder Metallurgy, Compaction, Sintering, Fatigue Life, Material Modeling, Finite Elements.

1. Introduction

Computational and mathematical based modeling for describing the mechanical behavior of components during fatigue testing process is recognized as providing significant contributions to improving reliability and quality of Powder Metallurgy (PM) parts and studying the durability and life of PM components (Riedel and Kraft, 2004). These techniques are helpful in predicting the location of failure of the component, stress distributions, cracks initiating during the fatigue loading. The major factors affecting the fatigue properties of PM materials are: density and pore distribution, composition, phase microstructure and post-sintering treatment (mechanical and/or thermal). Density has been recognized as having the most significant effect on fatigue strength (Sanderow et al., 1997), the steel composition is a minor factor, assuming a similar carbon content. Pores in sintered steels parts reduce the resisting section, cause local stress accumulation, and act as stress concentrators and crack initiation sites, thus their form and distribution are very important. In the density interval of 7.1 to 7.4 g/cm^3, fatigue limit increases approximately 5-10% per 0.1 g/cm^3 (Bergmark et al., 2002). An important density parameter for fatigue in PM materials is the Young's modulus, *E*. Under the assumption that the fatigue initiation is connected to a

critical strain, increased E permits a higher load before the local strain attains the critical value (Ericsson, 2003). To obtain a good estimate of the fatigue life, it is therefore primordial to accurately predict the density distributions of the different PM manufacturing processes, such as compaction and sintering. However, for constitutive laws to be accurate and successful, computer simulations should be also accompanied with a complete experimental database for validation. In this paper, these validation experiments comprise several test methods, such as powder material characterization, density measurements and fatigue testing of main bearing caps (MBCs).

2. Die Compaction

2.1 Compaction modeling

Die compaction is the first consolidation process of the PM press-sinter process. Here, a modified Drucker-Prager/Cap material model originally proposed by DiMaggio and Sandler (1971) for soils mechanics (Figure 1) is used to model the powder behavior during densification. The plastic flow is defined by two dissipation potentials that are respectively non-associated to the failure envelope F^e in the low pressure region, and associated to the cap yield surface F^c in the high pressure region:

$$F^e = \left|\underline{s} - \underline{\alpha}\right| - \kappa - d - p\tan\beta - f_t(p, p_a) = 0\,, \tag{1}$$

where β is the material's angle of friction and d is its cohesion strength, both function of the relative density ρ (Coube and Riedel, 2000). The failure yield surface is connected to the cap yield surface smoothly using a transition function f_t in the failure yield surface F_s. The cap hardening variable p_a is an evolution parameter that represents the volumetric plastic strain driven hardening/softening (Figure 1). At high densities (near fully dense material), the powder aggregate is described by a Mises type yield surface with isotropic hardening κ and kinematic hardening $\underline{\alpha}$. Therefore, for the stress state $p \geq p_a$, the cap surface is replaced by a Mises yield surface (Figure 1).

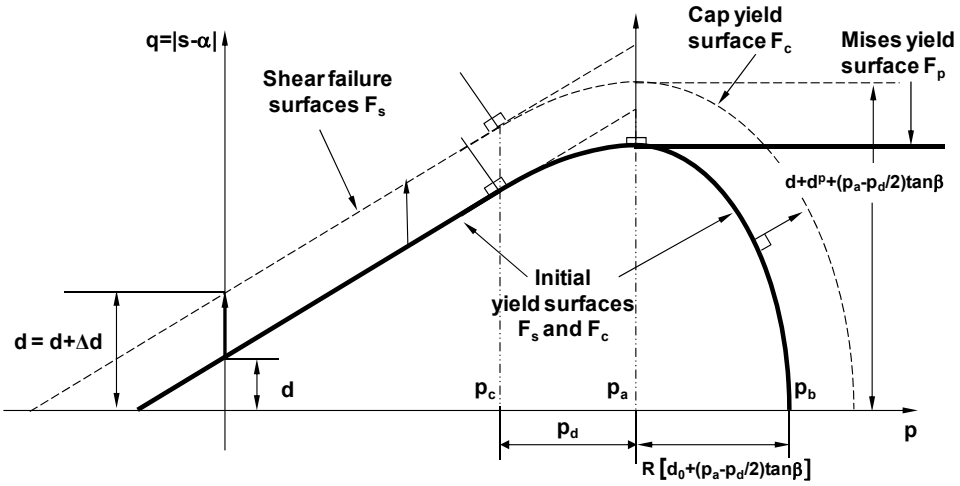

Figure 1. Modified Drucker-Prager/Cap Model: yield surfaces in the (*q*–*p*) plane.

The cap yield surface F^c has an elliptical shape in the meridional (q–p) plane and is written as

$$F^c = \sqrt{|s-\alpha|^2 - \frac{1}{R^2}[p-p_a]^2} - F_e(d,p_a) = 0, \tag{2}$$

where $R=R(\rho)$ is a the cap eccentricity that controls the shape of the cap. The evolution parameter p_a is also defined as a hardening parameter that controls the motion of the cap surface, and p_b defines the geometry of the cap surface. The ellipticity of the cap surface is determined by the material eccentricity parameter R that relates the hardening parameter p_a to p_b through the relation:

$$p_b = p_a + RF^e(p_a). \tag{3}$$

Sandler and Rubin (1979) proposed a relationship to define the evolution of the cap's motion, which is defined by the isotropic cap hardening rule

$$\bar{\varepsilon}^p_{vol} = W\left(1 - \exp\left[-c_1(p_b - p_{b|_0})^{c_2}\right]\right) \tag{4}$$

where p_b the hydrostatic compression yield stress, $\bar{\varepsilon}^p_{vol}$ is the effective volumetric plastic strain, W is the maximum plastic volumetric strain (at hydrostatic compression *'lockup'*), c_1 and c_2 are material parameters, and $p_{b|0}$ is the initial value of p_b.

2.2 Powder Characterization

A number of experimental tests and density measurements on a FC-0208 powder with 0.6% Acrawax have been performed to gather the data necessary for characterization and validation of the constitutive equations of compaction and sintering. Brazilian, compression and compressibility tests on cylindrical green samples were used to determine the failure line and cap surface at different densities (Coube and Riedel, 2000).

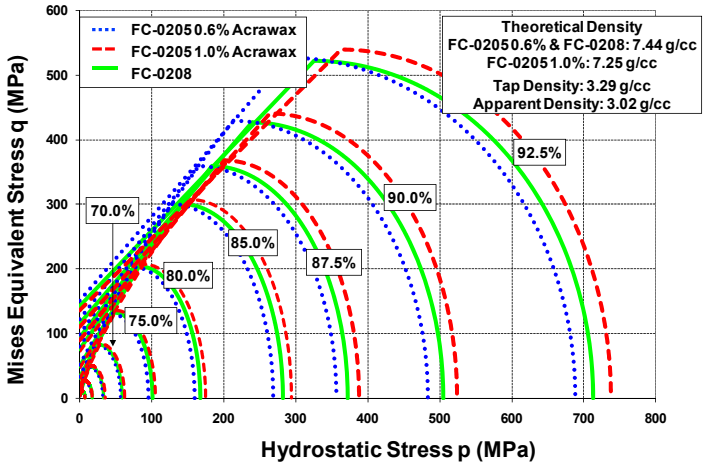

Figure 2. Isodensity curves in the p-q plan for FC-0205 and FC-0208 powders.

The resonant frequency method was applied to green compacts of different densities to determine the evolution of elastic properties during compaction. Figure 2 shows the equidensity lines in the (*p–q)* stress space, which correspond to the evolution of the Modified Drucker/Prager compaction model during densification.

2.3 Closed-die compaction of a main bearing cap

Using the Modified Drucker/Prager constitutive model for powder compaction, implemented in the user material subroutine VUMAT of Abaqus/Explicit, FE numerical analyses of a closed-die compaction of a MBC were performed. All dies and punches were assumed rigid, meshed with R3D4 elements, and moving tools were prescribed velocities as boundary conditions. The density before compaction is initialized with a non uniform distribution to account of the density gradient caused by the die wall friction during die filling. Wikman et al. (2000) estimated the coefficient of friction by combining an experiment with modeling of the experiment. They evaluated that the die-wall friction coefficient ranges from about 0.2 at high densities to 0.8 or even higher at low densities. In this calculation, the die-wall friction is given a constant value of μ=0.2, corresponding to friction conditions for a very high punch force. Figure 3 shows the density distribution of the compacted MBC in the die and before ejection for the FC-0208 powder.

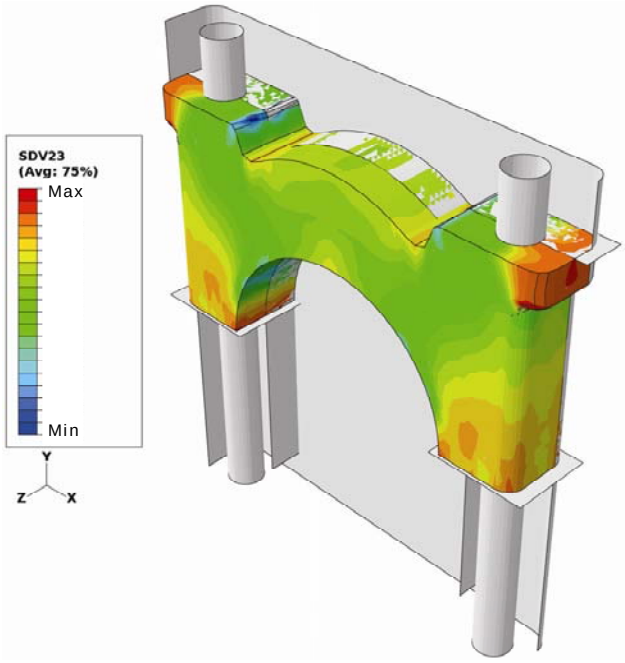

Figure 3. FEA simulation showing the MBC green density distribution at the end of compaction (in the die) for a FC-0208 0.6% Acrawax material.

The ejection phase is simply performed by a springback analysis in Abaqus/Standard, in which the MBC geometry and model were imported from Abaqus/Explicit. During this springback simulation, no further powder densification was considered, and the powder compact behavior was

assumed elastic. The Young's modulus was defined as a function of the green relative density ρ. During springback, the volume grows about 0.6% and dominant dimensional changes occur along the compacting direction as shown in Figure 4.

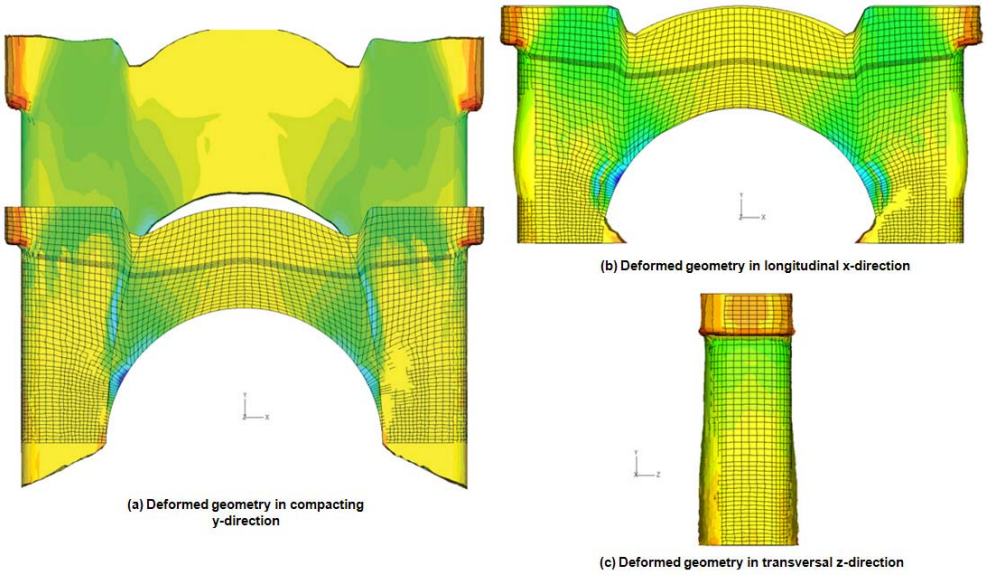

Figure 4. Geometry of MBC before springback (with mesh) and after springback (without mesh) with a deformation scale factor is 100.

Density in the MBC was measured using three different techniques: the immersion density technique based on the Archimedes' Principle, the image analysis method using optical microscopy and the X-Ray 2D CT technique. The MBC was cut into three layers, and each layer was cut into 20 pieces (Figure 5).

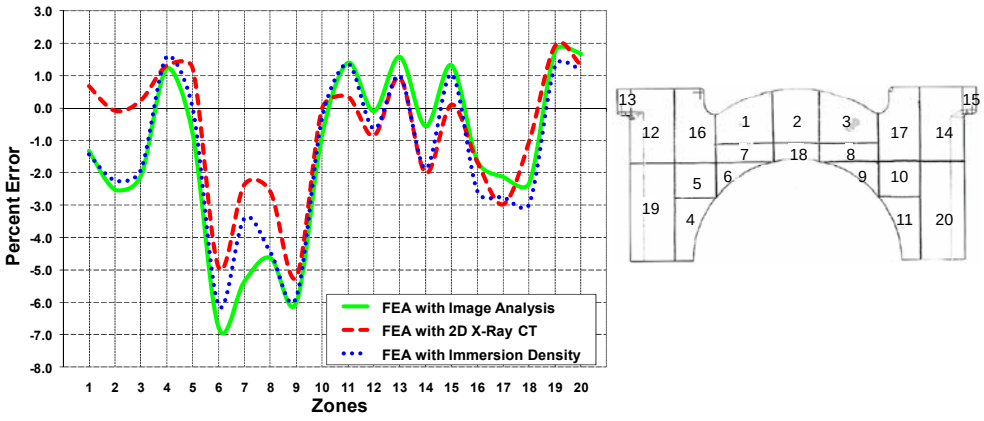

Figure 5. Density comparison in terms of percent error between numerical values and density measurements for 20 different zones.

An average density was measured for each piece. Group sets of elements were created in the post-processing analysis to represent the 20 pieces and the volume and mass of each element were summed up for each group set in order to calculate the average density. Figure 5 shows the comparison of numerical results with the three different density measurement techniques. Results are within 2-3 percent of error except for zones 6-9 where the density is much lower than measurements due to some numerical limitation of the finite element method, which cannot reproduce exactly the powder flow around the arch.

3. Sintering

3.1 Sintering Modeling

After compaction, sintering is the next basic step employed for producing PM parts. It consists of heating the powder compact material below the melting point to bond particles and increase the strength of PM parts. To study the creep of powder due to diffusional mass transport during sintering on the interparticle contacts, McMeeking and Kuhn (1992) proposed a macroscopic diffusional creep law in which the densification deformation rate is given by

$$\underline{D}^{di} = -\frac{1}{3}\frac{p+\sigma_s}{K_d}\underline{I} + \frac{q}{3\mu_d}\underline{n}\,. \tag{5}$$

where μ_d and K_d are the shear and bulk viscosities. In their approach, the diffusion was assumed to be very rapid on the free surface of the powder particles, so that the critical phenomenon was mass transport on the interparticle boundary. In these macroscopic continuum models, the microscopic diffusional forces that cause deformation during sintering were equivalent to a macroscopic stress, which is called sintering stress σ_s. The determination of this effective stress and its dependence on microstructural parameters, especially porosity, has been the focus of many works (Ashby, 1990; Beere, 1975; Skorohod, 1972). It is here function of the relative density ρ, the green relative densityρ_0, the grain size G, and γ the surface energy (Kwon et al., 2004).

The shear and bulk viscosities μ_d and K_d are averages over the microstructure of the deformation processes within the particles and on interparticle boundaries (German, 1996). Shear and bulk viscosities are common temperature-dependent material parameters used to describe the rheological behavior of wrought materials. However, for porous materials, material parameters continually change as the material densifies during sintering. Therefore, viscosity values measured from porous materials include this density effect and are thus called apparent viscosities. For a given temperature and density, the response of a porous body to strain rate to stress is linear. Therefore, the linearity of the viscous response of the porous body is maintained even though the apparent viscosity changes with density. Finally, the grain growth evolution under pressureless sintering can be written as (Kwon et al., 2004):

$$\dot{G} = k_0 \exp\left[-Q_G/RT\right]/G^2 \tag{6}$$

where k_0 is a material constant, Q_G the activation energy, and R the gas constant.

3.2 Sintering material characterization

To calibrate the FC-0208 sintering material parameters, a comparison between experimental dilatometer tests and numerical analysis on axial shrinkage was performed. The dilatometer

sintering tests are conducted on a cylindrical powder compact 0.5 inch diameter and 0.5 inch high with a green relative density of 0.60 percent. The numerical analysis is performed using axisymmetric elements (CAX4). The FC-0208 powder being mainly composed of iron, we then assumed the temperature-dependent linear thermal expansion coefficient of the FC-0208 powder compact to be equal to the one of pure iron.

3.3 Sintering of a main bearing cap

The sintering model was implemented in the user material subroutine UMAT using an implicit stress integration algorithm (Govindarajan, 1994). The sintering model was applied to the FC-0208 MBC to determine the mainly dimensional changes and the density variation. The analysis is performed in Abaqus/Standard using C3D8T elements. The material solution from the springback analysis was mapped to a new mesh using *MAP SOLUTION feature of Abaqus/Standard. The sintering temperature profile used by the automotive supplier during the MBC sintering process was applied in this analysis. The temperature is assumed to be uniformly distributed throughout the sintering process and therefore all the nodes have the same temperature evolution.

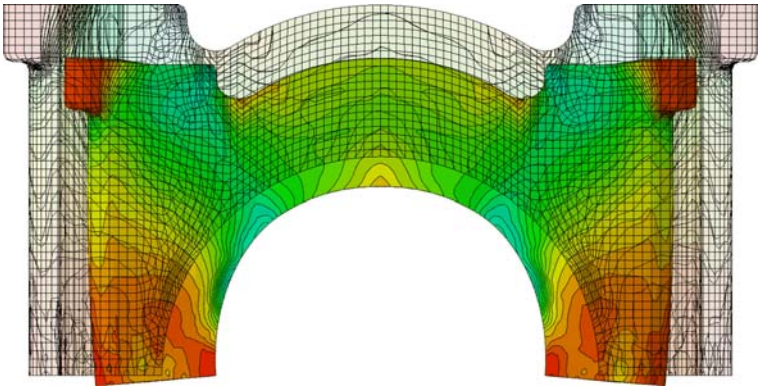

Figure 6. Density distribution and shrinkage of the MBC after sintering with a deformation scale factor of 100 (mesh of green part is shown as transparent).

Figure 6 shows the density distribution and the shrinkage of the MBC with respect to its initial shape at the beginning of the sintering process. The overall shrinkage was about 0.2-0.3% as observed by the automotive supplier. We can observe on the Figure 6 that the shrinkage is mostly uniform in all directions, with a very slight distortion of the arch shape and flat surfaces.

4. Fatigue life

4.1 Fatigue modeling

A MultiStage Fatigue (MSF) model initially developed for aluminum cast alloys (Horstemeyer et al., 2001; McDowell et al., 2003, Xue et al., 2007) and further enhanced for magnesium alloys (El Kadiri et al., 2006) is used here to predict the fatigue life of PM alloys. Since the PM alloys have similar microstructures and inclusions/defects, the modeling framework is inferred to be general enough to capture the fatigue behavior of these various PM alloys. However, minor revisions to the model were made to account for the porosity degradation of the elastic modulus and void coalescence as it relates more directly to the nearest neighbor distance.

The high fidelity multistage fatigue (MSF) model predicts the amount of fatigue cycling required to cause the appearance of a measurable crack, the crack size as a function of loading cycles. The model incorporates microstructural features to the fatigue life predictions for incubation, microstructurally small crack growth, and long crack growth stages in both high cycle and low cycle regimes.

The microstructure-based MSF model incorporates different microstructural discontinuities effect (pores, inclusions, etc.) on physical damage progression. This model partitions the fatigue life into three stages based on the fatigue damage formation and propagation mechanisms:

- crack incubation (INC),
- microstructurally small crack (MSC) and physically small crack (PSC) growth, and
- long crack (LC) growth.

The total fatigue life is decomposed into the cumulative number of cycles spent in several consecutive stages as follows:

$$N_{Total} = N_{INC} + N_{MSC} + N_{LC} \tag{7}$$

where N_{INC} is the number of cycles to incubate a crack at a micronotch that includes the nucleation of crack-like damage and early crack propagation through the region of the micronotch root influence; N_{MSC} is the number of cycles required for propagation of a microstructurally small crack with the crack length a. The crack range, $a_i < a <$ kDCS, with the DCS defined as the dendrite cell size, and k as the non-dimensional factor that is representative of a saturation limit for the encountering of a 3-D crack front with sets of microstructural discontinuities. The value N_{LC} is the number of cycles required for LC propagation for crack length a > (10–20) DCS, depending on the amplitude of loading and the corresponding extent of microplasticity ahead of the crack tip. This stage of crack extension is commonly characterized using standard fatigue crack growth experiments, da/dN versus ΔK. Finally N_{Total} is the total fatigue life**.**

To study the damage incubation life as a function of local plastic deformation, a modified Coffin–Mansion law was implemented based on the non-local maximum plastic shear strain, i.e.:

$$C_{INC} N_{INC}^{\alpha} = \beta = \frac{\Delta \gamma_{\max}^{p}}{2} \tag{8}$$

where β is the non-local maximum plastic shear strain amplitude around the inclusion calculated using an average of maximum plastic shear strain over an area approximately one percent of the inclusion area, and C_{INC} and α are the linear and exponential coefficients in the modified Coffin–Mansion law at the micronotch. The Paris Law is used to define the long crack growth rate (Paris et al., 1961). This implies that:

$$\frac{da}{dN} = A(\Delta K)^{m} \tag{9}$$

where A is the crack growth parameter and m the exponent in Paris Law, ΔK is the stress intensity factor, N the number of cycles, and log$A$ is defined as a constant.

The Multi-Stage Fatigue model was implemented in the Abaqus user output variable subroutine UVARM. It calculates the fatigue lives N_{INC}, N_{SC}, N_{LC} and N_{Total} at each material point using the

stress and strain amplitudes provided by the fatigue analysis, and store the values in user output variables UVAR*i*. The fatigue life values are interpolated with respect to porosity from fatigue experiments performed on samples of low and high porosities. Maximum values were set for each of the fatigue lives N_{INC}, N_{MSC}, and N_{LC} to avoid out of interest large fatigue number of cycles when plotting their values. The fatigue life for incubation constitutes most of the fatigue life, and the fatigue life due to small crack was essentially nonexistent because the large pores dominated the fatigue life. Once the incubation period is concluded and a fatigue crack is started, the crack length becomes the size of the pore plus the crack length.

4.2 Fatigue test fixture

Thirty MBCs manufactured with FC-0208 powder were recently submitted for fatigue testing. The staircase method, as specified in MPIF Standard 56, was implemented for this test. A testing fixture (Figure 7), designed to evaluate the fatigue strength of bearing caps, was used. As shown, the load, as in service, is applied at an angle of 10^o with the vertical axis (shown with arrows in Figure 1), and distributed along an arc length of 52.5^o (Ilia et al, 2003).

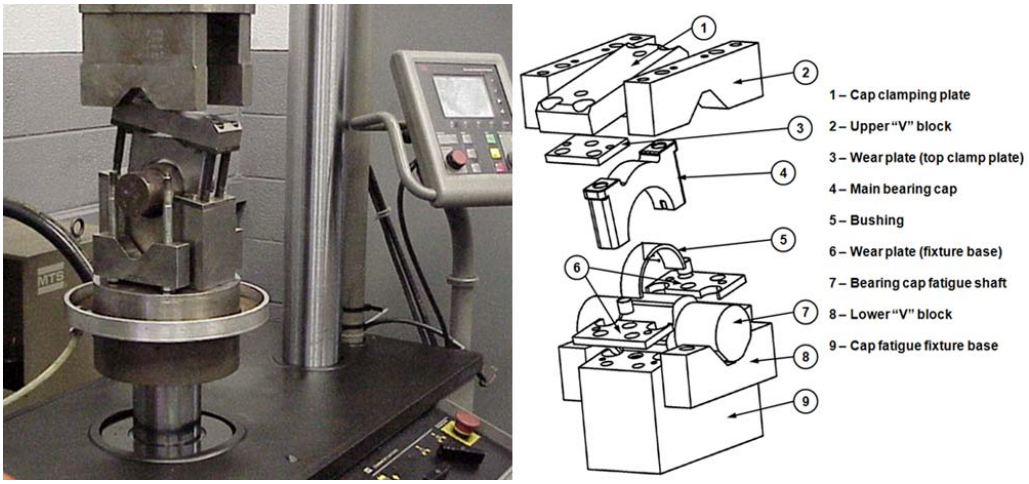

Figure 7. View of the MBC fatigue fixture used for tests.

A pre-loading torque of 60 lbf·ft was applied to each of the four bolts in order to make sure that the testing load was applied to the MBC. The tests were conducted at room temperature, in load control, on a MTS servohydraulic machine under a loading cycle consisting of a stress ratio $R \approx 0$ (a minimum load of 1,000 lbs was applied in order to maintain continuous contact during the entire duration of the test). Using the stair-case method, an incremental load step of 1,000 lbs up to 23,000 lbs was employed during the test. The fatigue tests were conducted by applying cyclic sine waveform loading vertically onto the shaft at of frequency of 40 Hz.

An MBC that did not have any crack indication after running 10^7 cycles was considered a runout. A failed bearing cap after a fatigue test exhibits a crack that typically starts at the area shown by the arrow on Figure 8 and continues toward the arch of the inner diameter. Most of the failures did not show a complete fracture through the arch. In most of the tests, a crack 1/8"–1/4" long was observed on both lateral sides of the cap after the test had completed 10^7 cycles (Ilia et al., 2003).

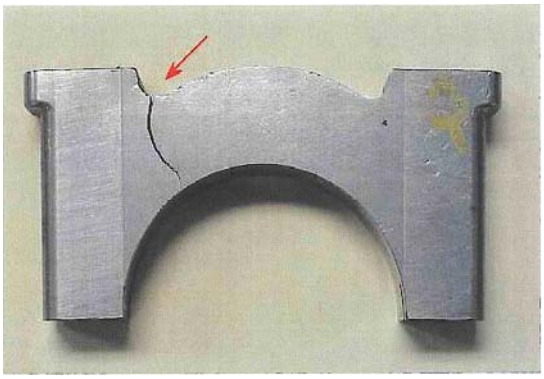

Figure 8. Partial Arc Failure in a failed MBC (Ilia et al, 2003).

Table 1 shows initial fatigue results after 10^7 cycles for different shaft loads with previous result tests obtained by the MBC automotive supplier. The experimental results are also compared to the FEA predictions discussed in the next section.

Table 1. Fatigue test results performed on the fatigue test fixture and FEA predictions.

Shaft Load (lbs)	Recent FC-0208 Test Results	Previous FC-0208 Test Result	MPP – Ilia et al., 2003	Fatigue FEA Analysis
18,000	N/A	N/A	Pass	Pass
19,000	Pass	N/A	Pass/Fail	Pass
20,000	Pass/Fail	Pass	Pass/Fail	Pass
21,000	Pass/Fail	Pass/Fail	Pass/Fail	Pass
22,000	Fail	Pass/Fail	Fail	Fail
23,000	N/A	Fail	N/A	Fail

4.3 Model Calibration of MSF Parameters

MBCs made from a PM manufacturing process have a non uniform density distribution as shown on Figure 3. To take into account this porosity level that can be ranging from 5% to about 20%, fatigue tests need to be performed at least at two different porosities. Using machined fatigue specimens from blank samples provided by the MBC automotive supplier, lower and upper bounds of the fatigue life were determined from strain-controlled low cycle fatigue tests on samples of respectively high and low porosities (Figure 9). The fatigue parameters were then calibrated on the low cycle fatigue curve and on its extrapolation for the high cycle regime was performed using the MSFfit software developed at CAVS. These fatigue parameters were finally applied in the MSF model to predict the fatigue life of the MBC in the fatigue simulations.

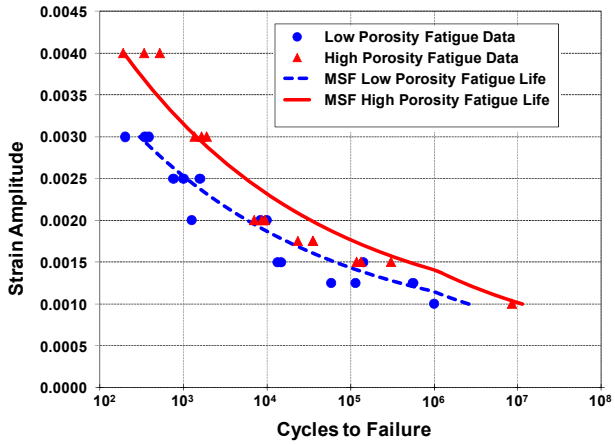

Figure 9. Strain Amplitude vs. Cycle to failure curve for the lower and higher bounds.

4.4 Fatigue simulations

To predict the fatigue life of the MBC, the fatigue fixture was modeled using Abaqus/Standard. The shaft was meshed as a rigid body with R3D4 rigid elements, while the other components of the fatigue fixture were modeled with C3D8R continuum brick elements with elastic properties. Using the feature *MAP SOLUTION in Abaqus/Standard, the density distribution was mapped from the PM compaction process analysis, more exactly from the springback analysis since the density variation during sintering was very small (0.2-0.3%) for the FC-0208 iron-based powder. The Young's modulus at each material point of the MBC is calculated within a material subroutine UMAT as a function of the porosity ϕ according:

$$E(\phi) = E_0 (1-\phi)^{\beta} \tag{10}$$

where E_0 is the Young's modulus of the raw material and β a shape parameter.

The fatigue FE analysis was decomposed into three steps to reproduce the in-service conditions of the fatigue fixture test:

- Bolt pre-loading: a pre-loading torque of 60 lbf·ft torque is applied to each of the four vertical bolts;
- Initial shaft loading: a minimum load of 1,000 lbs is applied upward on the shaft; and
- Shaft loading: the maximum load 23,000 lbs is linearly applied upward on the shaft.

The fatigue life using the MSF model was calculated in the 'shaft loading' step analysis only. The implementation of the MSF model into the user subroutine UVARM was called for all material calculation points of MBC elements. The subroutine calculated and saved in a COMMON block the effective strain and Mises stress during the two first step analyses. In the third step analysis, the subroutine calculated at the end of each increment the effective total strain amplitude $\Delta\varepsilon_{eff}$ and Von Mises stress amplitude $\Delta\sigma_{eq}$ using the last saved values in the previous step analysis:

$$\Delta\varepsilon_{eff} = \varepsilon_{eff}\,|_{Max\ Load} - \varepsilon_{eff}\,|_{1{,}000\,lbs} \tag{11}$$

and

$$\Delta\sigma_{eq} = \sigma_{eq}\,|_{Max\ \mathrm{Load}} - \sigma_{eq}\,|_{1{,}000\,lbs} \tag{12}$$

that are needed to determine the fatigues lives N_{INC}, N_{SC}, N_{LC} and N_{TOTAL}.

Figure 10 shows the density distribution of the Mises stress and its calculated amplitude in the third step analysis. The stresses are concentrated in the same region as the observed crack during fatigue tests (Figure 8). Also, locally high stresses are observed at the contact surface between the bushing and the inner diameter of the MBC arch. High stresses when two contacting bodies are deformed can be anticipated under a variety of circumstances, but in finite element analysis it typically occurs at contact nodes where contact pressures are highly concentrated. These high calculations of stresses at contact interfaces are here ignored to avoid unreliable and generally unrealistic fatigue life calculations.

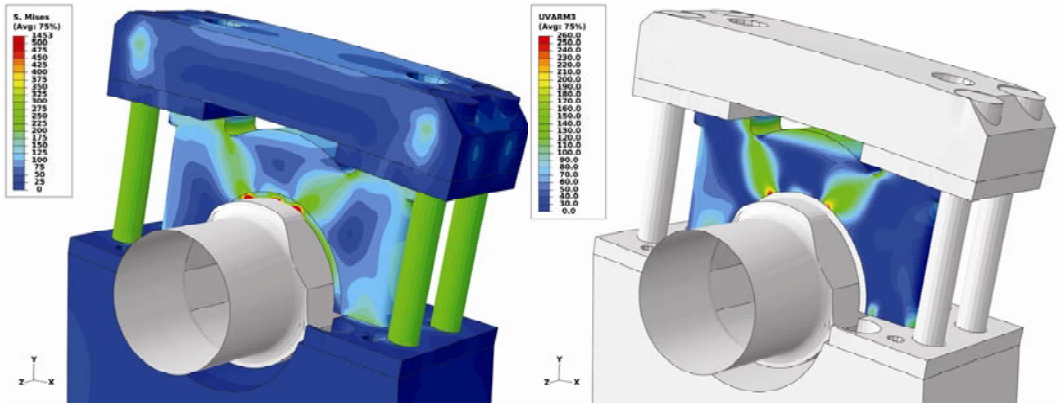

Figure 10. Mises stress and Mises stress amplitude distribution [MPa]: $\Delta\sigma_{eq}=\sigma_{eqMaxLoad}-\sigma_{eq1,000\ lbs}$ at a shaft load of 23,000 lbs.

Figures 11 and 12 show the contour plot of the incubation fatigue life N_{INC} and long crack fatigue life N_{LC}. If the singularities due to the contact nodes are ignored, the low values of incubation fatigue life N_{INC} (in red) indicate the location of the initial crack in MBC as it is observed during fatigue experiments (Figure 8). The values N_{INC} are lower than 10^7 cycles at this location for a shaft load of 22,000 lbs or more (see Table 1). The long crack fatigue life calculations are based on the Mises stress amplitude (Figure 10), and the contour plot displays low number of cycles along the crack path observed during the experimental fatigue tests (Figure 12). The MSF is able to predict long crack location on a single side only, contrarily to the apparent symmetry of the Mises stress amplitude (Figure 10), on which the fatigue life N_{LC} is based.

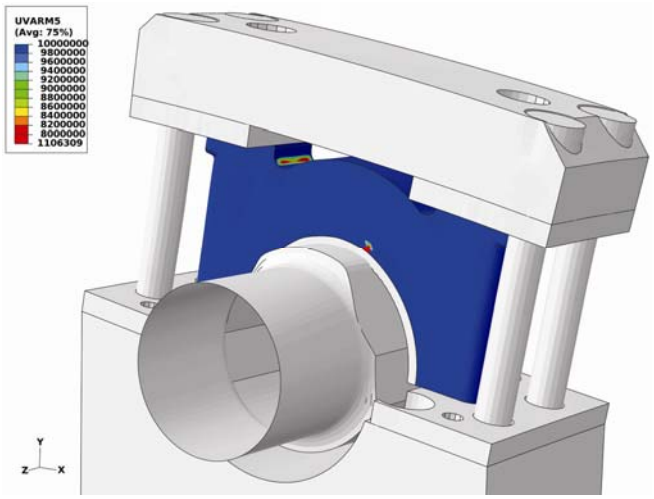

Figure 11. Number of Cycles N_{INC} for incubation at a shaft load of 23,000 lbs.

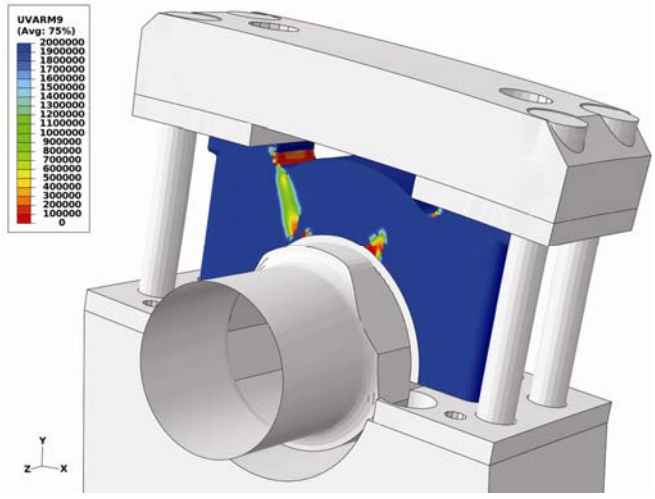

Figure 12. Number of Cycles N_{LC} for long crack at a shaft load of 23,000 lbs.

Table 1 shows the fatigue lives for different shaft loads. In automotive components, once a small crack occurs the component is considered failed and needs to be exchanged. As such, the long crack analysis is really not relevant for automotive structural components. Therefore, in this fatigue analysis only the incubation life is considered as relevant to predict the fatigue life of the FC0208 MBC. We consider the fatigue test is successful when the incubation fatigue life N_{INC} is greater than 10^7 cycles. The MSF analyses show good correlation in comparison with the experimental results in Table 1.

As such, this validation of the model brings confidence to the usage of the MSF model with heterogeneous porosity distributions since the correct location of the failure (Figure 11 and 12) and the correct number of cycles with associated loads were well predicted.

5. Conclusion

A modeling methodology was presented to capture the entire history of the density during the manufacturing press-sinter Powder Metallurgy (PM) process and predict the fatigue life of a PM part, the main bearing cap. The constitutive material and fatigue models were all implemented in several Abaqus user subroutines, such as VUMAT, UMAT and UVARM. Different material characterization, density measurements and fatigue tests were performed to calibrate and validate the modeling methodology. The Multi-Stage Fatigue (MSF) model showed its ability to accurately predict the fatigue life in PM automotive components, in which the density distribution must be accurately predicted due to its significant effects on fatigue properties. In the future, the goal will be to use this approach to predict the in-service performance and fatigue life of PM automotive components in general, and to optimize a PM component's design, performance, mass reduction, and cost savings.

6. Acknowledgments

The authors would like to acknowledge funding from the Center for Advanced Vehicular Systems at Mississippi State University and from USAMP Lightweight Materials Group. We also acknowledge guidance in this project from Howard I. Sanderow (Center for Powder Metallurgy Technology – CPMT), Russell A. Chernenkoff (Metaldyne), Jean C. Lynn (DaimlerChrysler), Shekhar G. Wakade (GM Powertrain), Glen Weber (Ford Motor Company), and Eric McCarty (Materials Technologies Consulting, L.L.C.).

7. References

1. Abaqus, User's Manual, Version 6.7, Hibbit, Karson & Sorensen, Inc., 2007.
2. Ashby, M.F., Sintering and isostatic pressing diagrams, Technical report, University of Cambridge, UK, 1990.
3. Beere, W., "The Second Stage Sintering Kinetics of Powder Compacts," Acta Metallurgica, Vol. 23, No. 1, pp. 139–145, 1975.
4. Bergmark, A., L. Alzati, and U. Persson, Fatigue crack initiation in PM steel, Advances in powder metallurgy & particulate materials, Metal Powder Industries Federation, Princeton (NJ). pp. 5-95/5-103, 2002.
5. Coube, O. and H. Riedel, "Numerical Simulation of Metal Powder Die Compaction with Special Consideration of Cracking", Powder Metallurgy, 2000, Vol. 43, No. 2, pp. 123–131.
6. DiMaggio, F.L. and I.S. Sandler, "Material Models for Granular Soils", Journal of Engineering Mechanics", ASCE, 1971, Vol. 97, EM3, pp. 935–950.
7. El Kadiri, H., Y. Xue, M.F. Horstemeyer, J.B. Jordon, J.B., and P.T. Wang, "Identification and modeling of fatigue crack growth mechanisms in a die-cast AM50 magnesium alloy," Acta Materialia, Vol. 54, No. 19, pp 5061–5076, 2006.

8. Ericsson, H., “Influence of Notches on Fatigue Behavior of PM Steels”, Masters’ Thesis, Department of Applied Physics and Mechanical Engineering Division of Engineering Materials. Luleå University of Technology. Sweden 2003:255 CIV Luleå 2003.
9. German, R.M., Sintering Theory and Practice, Wiley and Sons, 1996.
10. Govindarajan, R.M., and N. Aravas, “Deformation processing of metal powders: Part II – Hot isostatic pressing”, Int. J. Mech Sci., 1994, Vol. 36, No. 4, pp. 359–372.
11. Horstemeyer, M.F., J. Fan, and D.L. McDowell, “From Atoms to Autos: Part 2 Fatigue Modeling,” Sandia National Laboratories Report, SAND2001-8661, 2001b.
12. Ilia, E., M. O'Neill, J. Lee, J. Poirier, and S. St-Laurent, “Development of a Main Bearing Cap for an Inline 6 Cylinder Engine,” Advances in Powder Metallurgy and Particulate Materials, Part 9, pp. 9-22–9-35, 2003.
13. Kraft, T., and H. Riedel, “Numerical simulation of die compaction and sintering”, Powder Metallurgy, 2002, Vol. 45, No. 3, pp. 227–231.
14. Kwon, Y.S., Y. Wu, P. Suri, and R.M. German, “Simulation of the Sintering Densification and Shrinkage Behavior of Powder Injection Molded 17-4PH Stainless Steel,” Metal. Mater. Trans., 2004, Vol. 35 A, No. 1, pp. 257–263.
15. McDowell, D.L., K. Gall, M.F. Horstemeyer, and J. Fan, “Microstructure-Based Fatigue Modeling of Cast A356-T6 Alloy,” Engineering Fracture Mechanics, Vol. 70, pp.49–80, 2003.
16. McMeeking, R.M., and L.T. Kuhn, “A Diffusional Creep Law for Powder Compacts,” Acta Metallurgica and Materiala, Vol. 40, No. 5, pp. 961–969, 1992
17. Paris, P.C., M.P. Gomez, and W.E. Anderson, “A Rational Analytic Theory of Fatigue,” The Trend in Engineering, Vol. 13, pp. 9–14, 1961.
18. Riedel, H., and T. Kraft, Simulation in Powder Technology. In: D. Raabe, F. Roters, F. Barlat and L.-Q. Chen, Editors, Continuum Scale Simulation of Engineering Materials: Fundamentals – Microstructures – Process Applications, Wiley-VCH Verlag, pp. 657–674, 2004.
19. Sanderow, S., J.R. Spirko, and T.G. Friedhoff, “Fatigue Properties of P/M Materials: Relationship of RBF and AF results to material-processing parameters,” Advances in Powder Metallurgy and Particulated Materials, Metal Powder Industries Federation, Vol. 13, pp. 117—135, 1997.
20. Sandler, I.S., and D. Rubin, “An Algorithm and a Modular Subroutine for the Cap Model”, International Journal for Numerical and Analytical Methods in Geomechanics, Vol. 3, pp. 173–186, 1979.
21. Skorohod, V.V., “Rheological Basis of the Theory of Sintering,” Naukova Dumka, Kiev, 1972.
22. Wikman, B., N. Solimannezhad, R. Larsson, M. Oldenburg, and H.-A. Haggblad, “Wall friction coefficient estimation through modelling of powder die pressing experiment”, Powder Metallurgy, Vol. 43, No. 2, pp. 132–138, 2000.
23. Xue, Y., C.L. Burton, M.F. Horstemeyer, and D.L. McDowell, “Multistage Fatigue Modeling of Cast A356-T6 and A380-F Aluminum Alloys,” Metallurgical and Materials Transactions B, Vol. 38, pp. 601-606, 2007.